Electronic Supplementary Material (ESI) for Nanoscale Advances.

Supporting Information

Fluorescence excitation enhancement by waveguiding nanowires

Ivan N. Unksov[†, ‡], *Nicklas Anttu*[▽, ‡], *Damiano Verardo*[†, §], *Fredrik Höök*[||], *Christelle N. Prinz*[†], *Heiner Linke*[*, †]

[†]NanoLund and Solid State Physics, Lund University, Box 118, 22100 Lund, Sweden

[▽]Physics, Faculty of Science and Engineering, Åbo Akademi University, FI-20500 Turku, Finland

[§]AlignedBio AB, Medicon Village, Scheeletorget 1, 223 63 Lund, Sweden

[||]Department of Physics, Chalmers University of Technology, 41296 Gothenburg, Sweden

Section 1. Additional technical details of optics modelling

We assume that the photo-excitation-de-excitation cycle of a fluorophore is dominated by the time it takes for a fluorophore to get excited. Furthermore, we assume that the excitation probability of a fluorophore is proportional to the electric field strength squared, $|\mathbf{E}(r,z)|^2$, which shows circular symmetry for the circularly symmetric geometrical system and illumination condition, with $r = 0$ at the center of the nanowire cross-section and $z = 0$ at the top of the substrate (here, we have assumed that the excitation of the fluorophore does not show anisotropy with regard to the orientation of the local electric field). Thus, we assume that we are far from saturation in illumination power – this assumption was assessed experimentally by observing that the increase in bleaching rate stays linear with increasing illumination power in Figure S65 where saturation would show up as a sublinear power dependence.

We model the diffraction of incident light by solving the Maxwell equations with the finite-element method in Comsol Multiphysics similarly as in Ref. [1]. The optical response of the constituent materials is described by their respective refractive indexes *n*. For GaP, we use values from[2], for Al_2O_3 from[3], and for the surrounding water, we use $n = 1.33$.

We consider a plane wave at (vacuum) wavelength λ incident from a direction given by the polar angle θ_{inc} and azimuth angle ϕ_{inc} with polarization state *pol*. These incidence angles are defined such that $k_{z,inc} = k_0 n_{\mathrm{inc}} \cos(\theta_{\mathrm{inc}})$, $k_{x,inc} = k_0 n_{\mathrm{inc}} \sin(\theta_{\mathrm{inc}}) \cos(\phi_{\mathrm{inc}})$, and $k_{y,inc} = k_0 n_{\mathrm{inc}} \sin(\theta_{\mathrm{inc}}) \sin(\phi_{\mathrm{inc}})$. Here, n_{inc} is the (possibly wavelength-dependent) refractive index in the medium from which light is incident from, in our case water. For the polarization, we use two orthogonal states, chosen as *s* and *p* polarization here, where *s* polarization shows a zero value for

the *z* component of the electric field of the incident light (for the special case of $\theta_{\mathrm{inc}} = 0$ we choose the *s* polarization to be an incident plane wave whose electric field is *y* polarized).

We use a scattered field formulation. There, we use as background field $\mathbf{E}_{\mathrm{bg}}(\mathbf{r}, \lambda, \theta_{\mathrm{inc}}, \phi_{\mathrm{inc}}, pol)$ the analytically known solution for the electric field for the case of a planar oxide layer on top of the substrate, that is, without the nanowire. In the simulations, we have chosen the magnitude of the electric field of the incident plane wave such that for given θ_{inc}, ϕ_{inc}, and *pol* it is 1 V/m. In more detail, we use the Fresnel coefficients at the top and the bottom interface of the oxide to create the solution, which includes the geometrical series within the oxide layer for the infinitely many round-trips of partial scattering within the oxide layer. Next, we include the oxide-coated nanowire as the scatterer and solve for the scattered field $\mathbf{E}_{\mathrm{sc}}(\mathbf{r}, \lambda, \theta_{\mathrm{inc}}, \phi_{\mathrm{inc}}, pol)$. Then, the total field is given by $\mathbf{E}(\mathbf{r}, \lambda, \theta_{\mathrm{inc}}, \phi_{\mathrm{inc}}, \mathrm{pol}) = \mathbf{E}_{\mathrm{bg}}(\mathbf{r}, \lambda, \theta_{\mathrm{inc}}, \phi, \mathrm{pol}) + \mathbf{E}_{\mathrm{sc}}(\mathbf{r}, \lambda, \theta_{\mathrm{inc}}, \phi_{\mathrm{inc}}, pol)$.

For the wide-field illumination, we assume incoherent plane waves from within the numerical aperture NA of the objective, with $\theta_{\mathrm{NA}} = \arcsin\left(\frac{\mathrm{NA}}{n_{\mathrm{inc}}}\right)$ the maximum incident angle, such that the intensity of the electric field at location $\mathbf{r}$ is given by:

$$|\mathbf{E}(\mathbf{r}, \lambda)|^2 = \sum_{pol=s,p} \int_0^{\theta_{\mathrm{NA}}} \int_0^{2\pi} |\mathbf{E}(\mathbf{r}, \lambda, \theta_{\mathrm{inc}}, \phi_{\mathrm{inc}}, pol)|^2 \sin(\theta_{\mathrm{inc}}) d\phi_{\mathrm{inc}} d\theta_{\mathrm{inc}} \,/$$

$$\sum_{pol=s,p} \int_0^{\theta_{\mathrm{NA}}} \int_0^{2\pi} \sin(\theta_{\mathrm{inc}}) d\phi_{\mathrm{inc}} d\theta_{\mathrm{inc}}. \quad \text{(S1)}$$

With this choice for the normalization, $|\mathbf{E}(\mathbf{r}, \lambda)|^2 = 1 \left[\frac{\mathrm{V}}{\mathrm{m}}\right]^2$ corresponds to the same local intensity as on the fluorophore in the homogeneous liquid without nanowire, oxide, or substrate.

For the fluorophores around the nanowire, we consider

$$|\mathrm{E}(r, z, \lambda)|^2 = \int_0^{2\pi} |\mathbf{E}(x, y, z, \lambda)|^2 \, d\phi/(2\pi) \quad \text{(S2)}$$

where $x = r\cos(\text{ø})$ and $y = r\sin(\text{ø})$. Importantly, due to the circular symmetry of the nanowire, in the calculations, we can exchange this ø averaging into an averaging over ø already in Eq. (S1). Hence, a simulation for a given ø_{inc} gives all the information we need about the variation of the averaged field over the circumference of the nanowire at given *r* for all the possible incidence angles ø_{inc}. Thus, we need only to vary θ_{inc} and *pol* in the actual simulations. We performed the modelling with a step of 5 degrees in θ_{inc}, after initial test runs indicating that negligible differences occurred compared to a much finer, and computationally more costly, stepping at 1 degree.

For completeness, we introduce the terms $|\mathrm{E}_{\mathrm{NW}}(r,z)|^2$ and $\left|\mathrm{E}_{\mathrm{planar}}(z)\right|^2$ for a fluorophore in the vicinity of the nanowire and a flurophore on top of the planar substrate without the nanowire present.

In the modelling, we assume that the fluorophores reside in a Δ_{Fluor} = 10 nm wide layer, in water, on top of the oxide. We calculate then the bleaching rate modification, relative to the fluorophore in the liquid, as (note that the substrate/oxide interface is located at *z* = 0 with positive *z* above the substrate):

$$M_{\mathrm{NW}} = \frac{\int_{z=t_{\mathrm{oxide}}}^{z=t_{\mathrm{oxide}}+L} \int_{r=d/2+t_{\mathrm{oxide}}}^{r=d/2+t_{\mathrm{oxide}}+\Delta_{\mathrm{Fluor}}} |\mathrm{E}_{\mathrm{NW}}(r,z)|^2 r dr dz}{L[(d/2+t_{\mathrm{oxide}}+\Delta_{\mathrm{Fluor}})^2 - (d/2+t_{\mathrm{oxide}})^2]/2}$$

$$M_{\mathrm{Planar}} = \frac{\int_{z=t_{\mathrm{oxide}}}^{z=t_{\mathrm{oxide}}+\Delta_{\mathrm{Fluor}}} \left|\mathrm{E}_{\mathrm{planar}}(z)\right|^2 dz}{\Delta_{\mathrm{Fluor}}}$$

Then, from $M_{\mathrm{NW}}/M_{\mathrm{Planar}}$ we obtain the value to compare with experiments. Importantly, when we use $M_{\mathrm{NW}}/M_{\mathrm{Planar}}$ to quantify the bleaching rate modification, we do not need as input the actual illumination power or the bleaching rate in the test liquid for a given illumination power. Therefore, $M_{\mathrm{NW}}/M_{\mathrm{Planar}}$ is independent of the exact choice of the fluorophore, as long as it can be excited at λ and the fluorescence is detected by our optical system.

Note that M_{NW} depends on r_{NW} and t_{oxide} (also on L but that dependence is insignificant for $L \geq 1000$ nm at the modelled $\lambda = 640$ nm, see Figure S1), and M_{Planar} depends on t_{oxide}; furthermore, both depend on λ and NA.

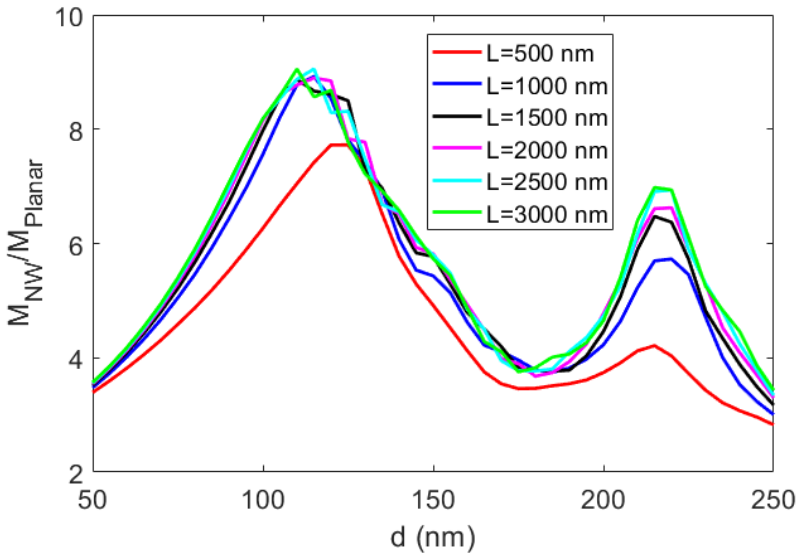

Figure S1. $M_{\mathrm{NW}}/\mathrm{M}_{\mathrm{Planar}}$ for varying L at NA = 1, λ = 640 nm, and t_{oxide} = 10 nm. The simulations are performed with a step of 5 nm in *d*.

Section 2. Modelling of wavelength dependence of the enhancement

At λ = 640 nm, n = 3.31 for GaP and 1.77 for Al_2O_3. At λ = 550 nm, n = 3.45 + i0.001 for GaP and 1.77 for Al_2O_3. At λ = 450 nm, n = 3.87 + i0.078 for GaP and 1.78 for Al_2O_3. The imaginary part of n, which gives to absorption, is negligible in GaP still at λ = 550 nm (the absorption length

in bulk GaP, given by $(4\pi \mathrm{Im}(n)/\lambda)^{-1}$, is 40 μm). However, at λ = 450 nm, the absorption length has decreased to 460 nm.

In Figure S2, we show the bleaching rate modification for these three excitation wavelengths. The peak that shows up at d = 115 nm for λ = 640 nm has shifted to d = 95 nm for λ = 550 nm and d = 70 nm for λ = 450 nm. This shift corresponds extremely well to the shifting to $d' = d[\lambda'/\lambda][\mathrm{Re}(n(\lambda))/\mathrm{Re}(n(\lambda'))]$ observed for diameter-dominated resonances in nanowires,[4] which predicts a shift to d = 95 nm and 69 nm (this equation originates from the assumption that for a given resonance, the optical path length around the circumference of the nanowire, which is proportional to $d\mathrm{Re}(n(\lambda))/\lambda$, should be kept constant to stay at the resonance when d and/or λ is varied).

In the simulations, the second peak at d = 220 nm at λ = 640 nm shifts to d = 180 nm at λ = 550 nm and d = 130 nm at λ = 450 nm. The prediction from the change in λ and Re(n) is a shift to d = 181 and 132 nm, respectively, in excellent agreement with the peak positions in the simulations. Notice that for λ = 450 nm, an additional higher order resonance shows up at d = 180 nm.

Based on these results, we see that by tuning λ we can in a predictable manner tune at which d the peak enhancement occurs (if we know at which d the peak occurs for a given λ, or at which λ the peak occurs for a given d).

Also, we see that for λ = 450 nm, the absorption in the GaP, through the non-negligible Im($\underline{n}$), causes a noticeable decrease in $M_{\mathrm{NW}}/\mathrm{M}_{\mathrm{Planar}}$ (black line) as compared to the results from simulation where Im(n) = 0 was set for GaP (magenta line).

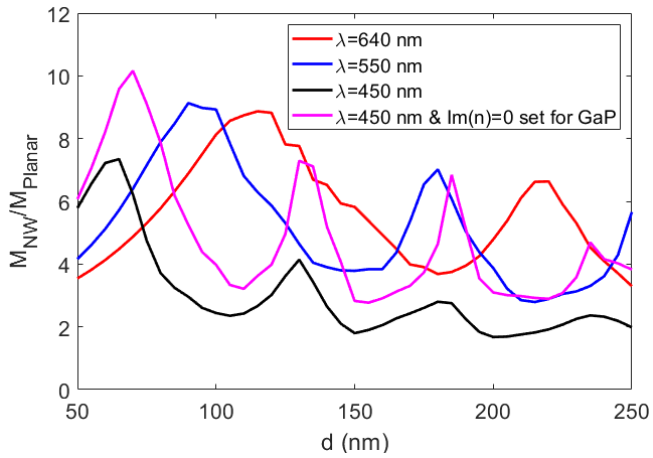

Figure S2. $M_{\mathrm{NW}}/M_{\mathrm{Planar}}$ for $L = 2000$ nm at NA = 1, and t_{oxide} = 10 nm. The simulations are performed with a step of 5 nm in *d*.

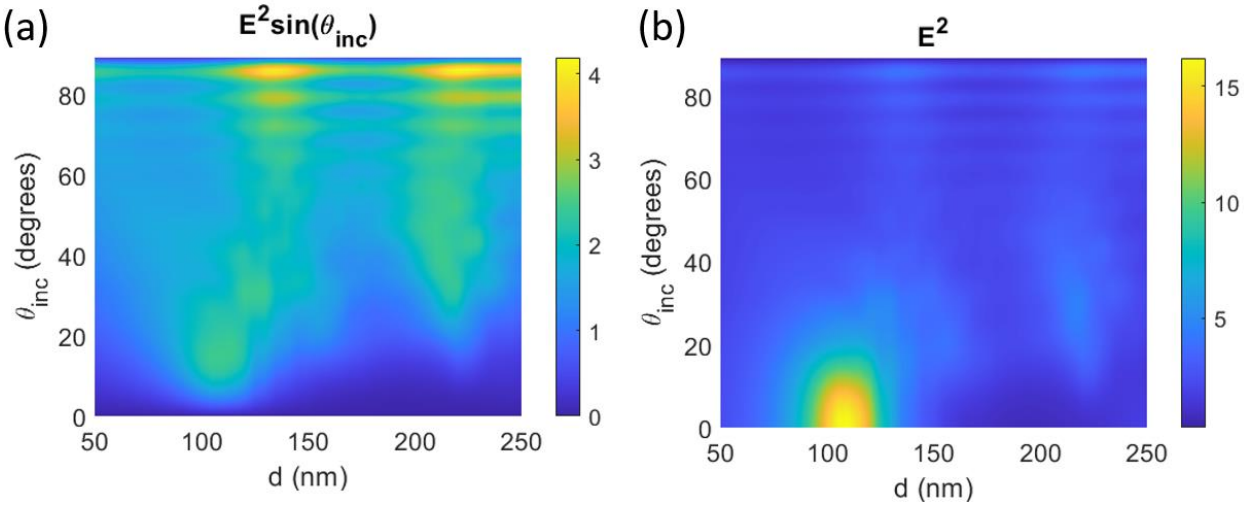

Figure S3. Enhancement for varying incidence angle for $L = 2000$ nm at λ = 640 nm, and t_{oxide} = 10 nm. The simulations are performed with a step of 5 nm in *d*. Here, we show in (a) the quantity $\frac{dM_{NW,\theta_{\mathrm{inc}}}(\theta_{\mathrm{inc}})}{\mathrm{d}\theta_{\mathrm{inc}}} = \frac{\int_{z=t_{\mathrm{oxide}}}^{z=t_{\mathrm{oxide}}+L}\int_{r=d/2+t_{\mathrm{oxide}}}^{r=d/2+t_{\mathrm{oxide}}+\Delta_{\mathrm{Fluor}}}\sum_{pol=s,p}\frac{1}{2}\int_0^{2\pi}|\mathbf{E}(\mathbf{r},\lambda,\theta_{\mathrm{inc}},\phi_{\mathrm{inc}},pol)|^2\sin(\theta_{\mathrm{inc}})d\phi_{\mathrm{inc}}rdrdz}{\frac{L\left[(d/2+t_{\mathrm{oxide}}+\Delta_{\mathrm{Fluor}})^2-(d/2+t_{\mathrm{oxide}})^2\right]}{2}} = \sin(\theta_{\mathrm{inc}})\frac{\int_{z=t_{\mathrm{oxide}}}^{z=t_{\mathrm{oxide}}+L}\int_{r=d/2+t_{\mathrm{oxide}}}^{r=d/2+t_{\mathrm{oxide}}+\Delta_{\mathrm{Fluor}}}\sum_{pol=s,p}\frac{1}{2}\int_0^{2\pi}|\mathbf{E}(\mathbf{r},\lambda,\theta_{\mathrm{inc}},\phi_{\mathrm{inc}},pol)|^2d\phi_{\mathrm{inc}}rdrdz}{L[(d/2+t_{\mathrm{oxide}}+\Delta_{\mathrm{Fluor}})^2-(d/2+t_{\mathrm{oxide}})^2]/2}$. Note that $M_{NW} = \int_0^{\theta_{\mathrm{NA}}}\left(dM_{NW,\theta_{\mathrm{inc}}}/\mathrm{d}\theta_{\mathrm{inc}}\right)\mathrm{d}\theta_{\mathrm{inc}}$. In (b), we show $\frac{\int_{z=t_{\mathrm{oxide}}}^{z=t_{\mathrm{oxide}}+L}\int_{r=d/2+t_{\mathrm{oxide}}}^{r=d/2+t_{\mathrm{oxide}}+\Delta_{\mathrm{Fluor}}}\sum_{pol=s,p}\frac{1}{2}\int_0^{2\pi}|\mathbf{E}(\mathbf{r},\lambda,\theta_{\mathrm{inc}},\phi_{\mathrm{inc}},pol)|^2d\phi_{\mathrm{inc}}rdrdz}{L[(d/2+t_{\mathrm{oxide}}+\Delta_{\mathrm{Fluor}})^2-(d/2+t_{\mathrm{oxide}})^2]/2}$ that corresponds to the electric field enhancement for varying incidence angle.

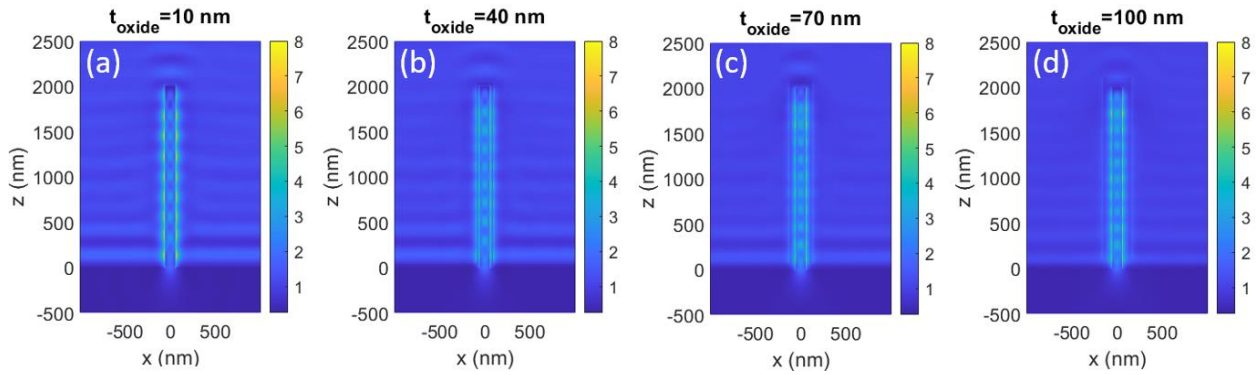

Figure S4. Same as Figure 1 b for t_{oxide} = 10 nm in (a), but here additionally also for (b) t_{oxide} = 40 nm, (c) t_{oxide} = 70 nm, and (d) t_{oxide} = 100 nm.

Section 3. Photobleaching rate, excitation enhancement and intensity measurements

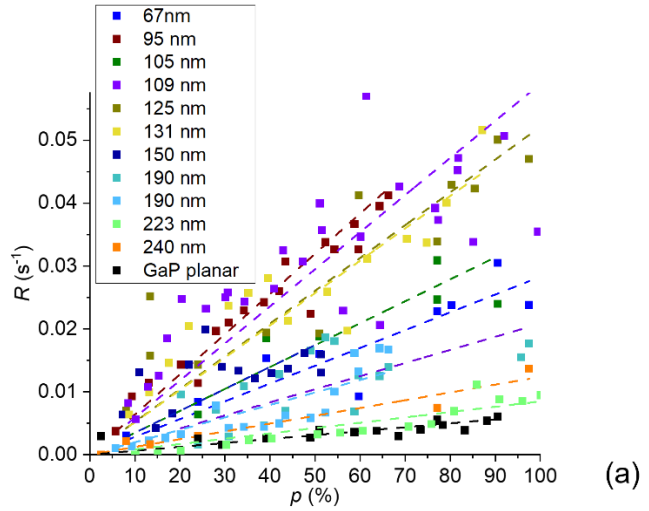

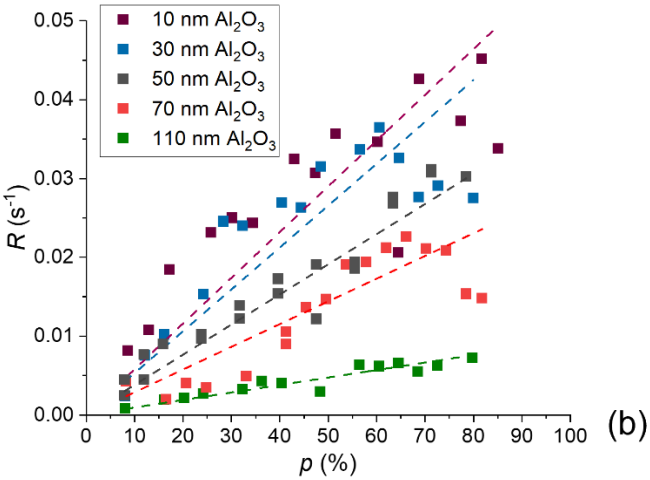

Figure S5. Photobleaching rates for (a) planar GaP and NWs of varied d with t_{oxide} = 10 nm Al_2O_3; (b) NWs of d = 109±10 nm and varied Al_2O_3 thickness.

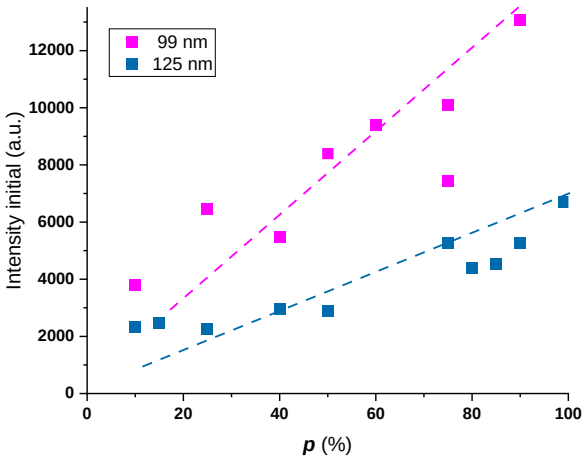

Figure S6. Fluorescence intensity at the onset of photobleaching at varied excitation power for two NW diameters. Intensities were recorded at or normalized to identical imaging conditions (exposure and the like).

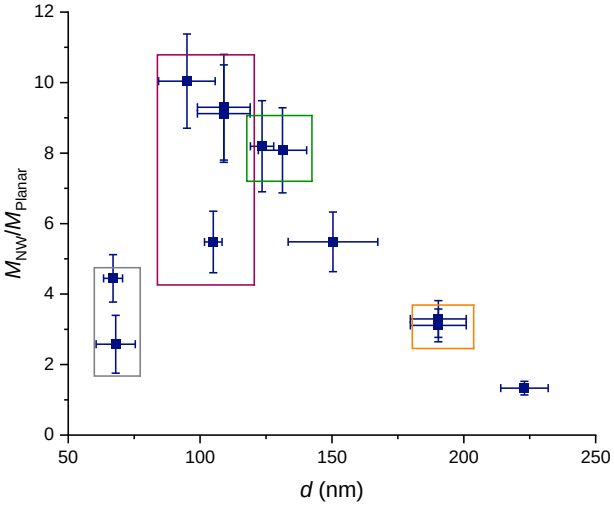

Figure S7. Experimentally measured photobleaching rate enhancement for NWs of varied d with t_{oxide} = 10 nm before averaging between samples of similar diameter (averaged datapoints are in rectangles). Uncertainties are assumed as the measurement uncertainty along y-axis, and diameter variation in the sample (Table S1). The data after averaging is shown in Figure 3.

Section 4. Nanowire growth

GaP (111)B wafers were used as growth substrates. The seeding particles were deposited on a GaP wafer from aerosol. MOVPE growth was carried out at Aix 200/4 (Aixtron AG) and started

with axial growth at 480 °C to reach a desired length, followed by radial growth at 600 °C to increase the NW diameter from 50 nm (the diameter after axial growth equals that of the seed particle) to a desired value. Reagents for the growth are phosphine (PH_3), trimethylgallium ($Ga(CH_3)_3$) and HCl. The dimensions of NWs were measured with SEM Hitachi SU8010 (Hitachi Ltd). Since the NWs are tapered, we assumed the characteristic diameter of a NW as measured at its half-length (see the diameters in Figure S8).

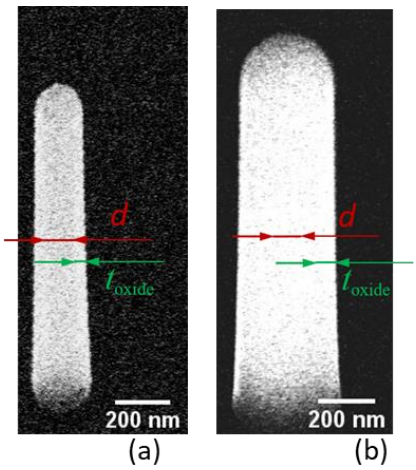

Figure S8. SEM image of vertical NWs with d = 109±10 nm and t_{oxide} of (a) 30 nm and (b) 115 nm on GaP substrate. Samples observed under 30° tilt from top view so that the apparent NW length is half of the actual length.

Section 5. Sample preparation, imaging and image segmentation

For imaging, GaP substrates with NWs were glued with double-sided sticky tape in ibidi 6 channel slides and sealed with a glass coverslip (#1).

Nikon TE2000-U microscope with Nikon Fluor 60X/1.00 DIC water immersion objective was used with installed quad-band filterset (Semrock, 405/488/561/635 nm BrightLine quad-edge laser-flat dichroic beamsplitter, 390/482/563/640 nm BrightLine quad-band bandpass filter, 446/523/600/677 nm BrightLine quad-band bandpass) and EMCCD camera Andor iXON Life 897 (Andor Oxford Instruments). Fluorescence was excited with OBIS 640 nm LX 100 mW laser (see

Figure S9 for the beam profile). Prior to imaging, laser excitation power was routinely calibrated using power meter Thorlabs PM100D. In our data, 100 % excitation power corresponds to 359 µW, as measured when the power meter is placed on top of the used objective, in the light path within the microscope.

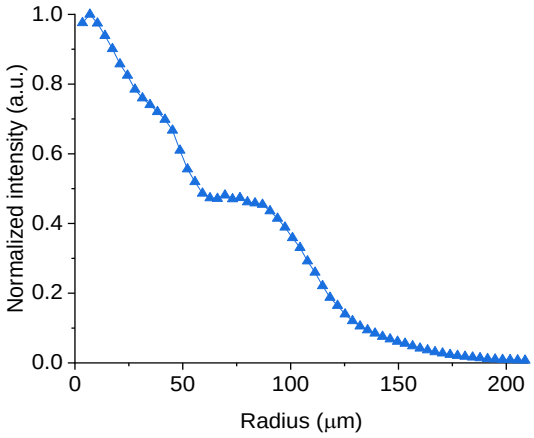

Figure S9. Profile of the laser beam entering the objective. The profile was measured with a CMOS camera Thorlabs Zelux™ 1.6 MP and plotted using the Radial Profile Extended plugin for ImageJ (http://questpharma.u-strasbg.fr/html/radial-profile-ext.html).

We did not measure the effective NA that the objective (nominal NA = 1) exhibits when used with the laser. Such an effective-NA measurement could be performed by measuring fluorescence interference oscillations[5] which however requires a specialized setup. Another method, possible for objectives with NA > 1 but not for our NA = 1 objective, utilizes the total internal reflection angle for back focal plane observation of angular distribution of fluorescence[6,7]. Yet another alternative is precise interferometric measurements [8].

Image segmentation in ImageJ[9] after drift correction was performed as follows, not on the images used for measurements but on duplicates of those: we subtracted the background, then applied a sharpening and/or blurring kernel to facilitate thresholding. Depending on the sample, two different methods for threshold-based identification of sparsely located NWs were used. For

samples with NW density of 0.5 μm^{-1}, we typically used Otsu[10] automatic thresholding. For less dense samples (0.2 μm^{-1}, see Table S1 for the densities of all samples), we typically used Huang automatic thresholding[11]. We adjusted additional restrictions on circularity and size of selected spots to select predominantly single NWs (Figure S10), filtering out the close-standing ones that merge in a single blob, as well as debris.

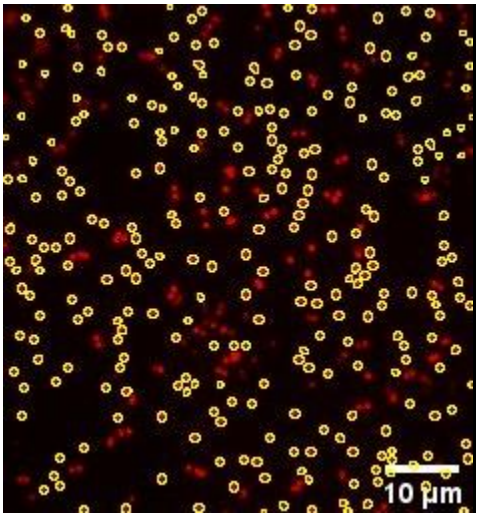

Figure S10. Fluorescence on NWs. In yellow – areas of NWs seen as diffraction limited spots, from which average intensity was taken for the calculation of *R*.

d (nm)	L (µm)	Density (NWs/µm^2)
67 ± 4	2.4 ± 0.0	0.5
68 ± 7	2.4 ± 0.2	0.5
95 ± 11	2.2 ± 0.1	0.5
99 ± 13	2.3 ± 0.1	0.5
105 ± 3	1.8 ± 0.3	0.5
109 ± 10	1.7 ± 0.1	0.2
124 ± 4	2.5 ± 0.1	0.5
131 ± 9	2.6 ± 0.1	0.2
150 ± 17	2.3 ± 0.2	0.2
190 ± 11	2.8 ± 0.1	0.5
223 ± 9	2.2 ± 0.2	0.2

Table S1. Density and length of the NWs in the study. Samples with similar (±10 nm) diameter, data for which were averaged in Figure 3, are color highlighted.

Section 6. Refractive indexes and absorbance of GaP compared with other III-V materials

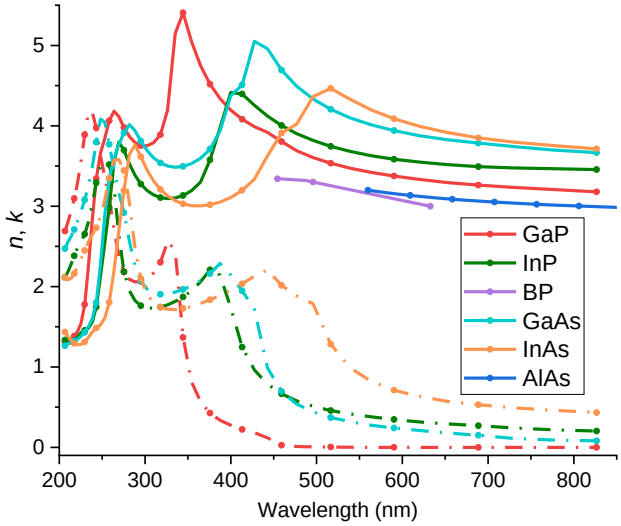

Figure S11. Refractive indexes n (solid lines) and extinction coefficients k (dashed lines) for some III-V semiconductor materials typically used for NWs. Values are from Refs. [2,12–14].

References

(1) Anttu, N.; Mäntynen, H.; Sorokina, A.; Kivisaari, P.; Sadi, T.; Lipsanen, H. Geometry Tailoring of Emission from Semiconductor Nanowires and Nanocones. *Photonics* **2020**, *7* (2), 23, DOI: 10.3390/PHOTONICS7020023.

(2) Aspnes, D. E.; Studna, A. A. Dielectric Functions and Optical Parameters of Si, Ge, GaP, GaAs, GaSb, InP, InAs, and InSb from 1.5 to 6.0 EV. *Phys Rev B* **1983**, *27* (2), 985–1009, DOI: 10.1103/PhysRevB.27.985.

(3) Dodge, M. J. "Refractive Index." In *Handbook of Laser Science and Technology, Volume IV, Optical Materials: Part 2*; Weber, M. J., Ed.; CRC Press: Boca Raton, 1986; p 30, DOI: 10.1201/9781003067955.

(4) Anttu, N.; Xu, H. Q. Efficient Light Management in Vertical Nanowire Arrays for Photovoltaics. *Opt Express* **2013**, *21* (S3), A558, DOI: 10.1364/oe.21.00a558.

(5) Müller, M.; Brakenhoff, G. J. Characterization of High-Numerical-Aperture Lenses by Spatial Autocorrelation of the Focal Field. *Opt Lett* **1995**, *20* (21), 2159, DOI: 10.1364/ol.20.002159.

(6) Zhang, B.; Zhang, C. Implementation of BFP-Typed Apertometer: Reference Location and Accuracy. *IEEE Trans Instrum Meas* **2021**, *70*, 7004308, DOI: 10.1109/TIM.2021.3077990.

(7) Dai, L.; Gregor, I.; von der Hocht, I.; Ruckstuhl, T.; Enderlein, J. Measuring Large Numerical Apertures by Imaging the Angular Distribution of Radiation of Fluorescing Molecules. *Opt Express* **2005**, *13* (23), 9409, DOI: 10.1364/opex.13.009409.

(8) Lei, F.; Dang, L. K. Measurement of the Numerical Aperture and F-Number of a Lens System by Using a Phase Grating. *Appl Opt* **1993**, *32* (28), 5689, DOI: 10.1364/ao.32.005689.

(9) Schindelin, J.; Arganda-Carreras, I.; Frise, E.; Kaynig, V.; Longair, M.; Pietzsch, T.; Preibisch, S.; Rueden, C.; Saalfeld, S.; Schmid, B.; Tinevez, J. Y.; White, D. J.; Hartenstein, V.; Eliceiri, K.; Tomancak, P.; Cardona, A. Fiji: An Open-Source Platform for Biological-Image Analysis. *Nat Methods* **2012**, *9* (7), 676–682, DOI: 10.1038/nmeth.2019.

(10) Otsu, N. A Threshold Selection Method from Gray-Level Histograms. *IEEE Trans Syst Man Cybern* **1979**, *9* (1), 62–66, DOI: 10.1109/tsmc.1979.4310076.

(11) Huang, L. K.; Wang, M. J. J. Image Thresholding by Minimizing the Measures of Fuzziness. *Pattern Recognit* **1995**, *28* (1), 41–51, DOI: 10.1016/0031-3203(94)E0043-K.

(12) Aspnes, D. E.; Kelso, S. M.; Logan, R. A.; Bhat, R. Optical Properties of AlxGa1−x As. *J Appl Phys* **1998**, *60* (2), 754, DOI: 10.1063/1.337426.

(13) Fern, R. E.; Onton, A. Refractive Index of AlAs. *J Appl Phys* **2003**, *42* (9), 3499, DOI: 10.1063/1.1660760.

(14) Wettling, W.; Windscheif, J. Elastic Constants and Refractive Index of Boron Phosphide. *Solid State Commun* **1984**, *50* (1), 33–34, DOI: 10.1016/0038-1098(84)90053-X.